Contents lists available at ScienceDirect

Theoretical and Applied Fracture Mechanics

journal homepage: http://ees.elsevier.com

Influence of non-homogeneous microstructure on hydrogen diffusion and trapping simulations near a crack tip in a welded joint

A. Díaz [a], I.I. Cuesta [a], C. Rodríguez [b], J.M. Alegre [a]

[a] University of Burgos, Escuela Politécnica Superior, Avenida Cantabria s/n, 09006 Burgos, Spain
[b] University of Oviedo. Campus Universitario, EPI, 33203 Gijón, Spain

ARTICLE INFO

Keywords
Hydrogen embrittlement
Fracture Mechanics
Hydrogen diffusion
Welding
Finite Element simulation

ABSTRACT

Hydrogen assisted fracture near welds is the result of a combination of microstructural changes and the accumulation of hydrogen. With the aim of predicting local hydrogen concentrations, hydrogen redistribution near a crack tip is simulated using a Boundary Layer approach and diffusion modelling is modified by trapping phenomena. The simulated non-homogeneous geometry includes layers that reproduce weld metal, heat affected zones and base metal of a 2.25Cr-1Mo steel; mechanical and diffusion properties have been extracted from references. The hydrogen transport model here considered involves a stress dependency that affects local concentrations; thus, the possible interaction between constraint effects associated to a graded material with hydrogen entry and transport is studied. Results show that the constraint effect is not significative for the loading and for the widths assigned to the weld and the heat affected zones (2.5 to 5 mm); however, for the HAZ-centred crack, a higher hydrostatic peak and the corresponding increase in lattice hydrogen are found. A two-type trapping process is also simulated to reproduce simultaneously the effect of dislocation trapping and microstructure delayed diffusion. Hydrogen is weakly trapped in dislocations and it is added to the lattice concentration to obtain a measure of diffusible hydrogen near a crack tip while effective diffusivity is strongly reduced by deeply trapped hydrogen. Differences between environmental or internal hydrogen sources are expected to be more accurately captured because stress-dependent boundary conditions have been implemented for hydrogen uptake.

1. Introduction

The failure of components under hydrogen environments is a common issue in many fields, leading to extensive research efforts to prevent and/or predict this phenomenon. Hydrogen-related failures can occur through various mechanisms, e.g. hydrogen damage at high temperature or blistering, but one of the most challenging process is embrittlement. Some theories have been proposed to explain micro-mechanisms whereby hydrogen reduces fracture toughness in metals and alloys: hydrogen-enhanced decohesion or hydrogen-enhanced localised plasticity are two paradigmatic mechanisms that have been supported by experimental and theoretical arguments [1–6]. Since micro-mechanisms are not yet completely understood [7], a robust unique physically-based model that is able to simulate hydrogen assisted fracture is hard to define.

Besides hydrogen damage, hydrogen transport, including surface phenomena and bulk diffusion, constitutes a fundamental process for predicting embrittlement [8]. Transport modelling is also challenging because the light hydrogen atom is subjected to many deviations from ideal diffusion [9]. The microstructural and mechanical influence on hydrogen transport has been addressed so the traditional Fick's laws have been modified to account for trapping and drifted diffusion.

Weldments are typical locations in which hydrogen assisted fracture must be assessed. The combination of residual stresses and microstructural changes that characterises welding critically affects hydrogen accumulation and cracking. Hydrogen is retained in lattice defects such as dislocations, grain boundaries, inclusions or vacancies. Some authors have demonstrated by first principles calculations that hydrogen diffusion depends on the crystal phase [10], which is experimentally confirmed [11], and that grain size strongly affects trapping [12]. Grain size dependency is partly explained by grain boundary trapping caused by the misorientation and by the accumulation of dislocations [13]. Joints are subjected during welding to temperature variations that induce thermal gradients and, consequently, microstructural changes. Additionally, different grain sizes are found along the heat affected zone (HAZ) [14]. The complexity of these non-homogeneous regions hinders an accurate prognosis of diffusion and trapping phenomena for welded joints exposed to hydrogen environments.

Finite Element predictions of microstructure, grain size and residual stress distributions through a welded joint require a complex implementation of coupled heat transfer–mechanical schemes [15]. To obtain accurate results, the temperature dependence of steel properties must be included, both for the elastic–plastic response [16,17] and for the thermal behaviour [18]. The strain induced by phase transformation can also be added to the volumetric strain produced by thermal expansion [19]. Additionally, a heat input modelling strategy must be chosen to simulate the thermal flux that is acting as a source during each pass [20]. The use of specialised welding software is also possible

https://doi.org/10.1016/j.tafmec.2020.102879
Received 2 October 2020; Received in revised form 8 December 2020; Accepted 16 December 2020
Available online xxx
0167-8442/

to automatize the process [21]. Other authors have used a simplified eigenstrain method for introducing residual stresses produced in a weld. This method has been successfully applied to the study of ductile and brittle fracture in welds [22–26]. Due to the complexity of thermo-mechanical simulations and phase transformation models, residual stresses are neglected here –which is usually assumed after a post-weld heat treatment (PWHT)– and microstructure is idealised by considering three layers with different mechanical and diffusion-related properties.

Embrittlement of welds has been experimentally studied by many authors considering different approaches to spatially resolve susceptibility of different microstructures and regions. Wu et al. (2019) [27] studied stress corrosion behaviour of different HAZ subregions in a bainite high-strength low-alloy (HSLA) steel, finding that embrittlement is more pronounced in the coarse-grained heat affected zone (CG-HAZ). Even though inter-critical (IC) and fine-grained (FG) regions present a higher amount of trapping sites due to the number of boundaries (prior austenite grains, lath bainite and martensite/austenite), the CG-HAZ shows a brittle behaviour due to its microstructure and the high dislocation accumulation. The interaction between hydrogen transport and damage micro-mechanisms requires a double characterisation: (i) modification of mechanical properties such as elongation, fracture toughness or fatigue resistance, is quantified by testing specimens in a hydrogen environment or after precharging; (ii) diffusion behaviour is characterised typically by electro-permeation tests in which solubilities and apparent diffusivities are measured. Zhang et al. (2017) [28] studied HAZ simulated specimens of a X80 pipeline steel and performed both gaseous permeation and slow strain rate tension tests (SSRT) in H_2 environment, confirming a higher embrittlement in the CG-HAZ; apparent diffusivities from gaseous permeation showed that $D_{app}^{CG-HAZ} > D_{app}^{FG-HAZ} > D_{app}^{IC-HAZ}$. Grain boundary trapping can explain this result since fine-grained regions comprise a higher number of boundaries. In contrast, some authors [29] have found that diffusion delay is more pronounced in CG-HAZ. Zafra et al. (2020) [29] explained this phenomenon in a 42CrMo4 considering that the microstructure in the CG-HAZ is more distorted due to the higher temperature decrease so trapping effects can be larger in comparison to fine-grained regions. In that study, the CG-HAZ also showed a high embrittlement index (50%) for notched H_2-charged specimens tested at slow displacement rates. Song et al. (2018) [30,31] showed that fracture toughness reduction happened both in the base metal and in the welded zone of a 2.25Cr-1Mo-0.25 V steel, but it was less critical in the base metal due to the finer grain size so grain boundary trapping limits hydrogen transport to the fracture process zone. Pereira et al. (2015) [32] compared base metal (BM), weld metal (WM) and HAZ of a welded joint in a 2.25Cr-1Mo-0.25 V steel using both electrochemical permeation at room temperature and gaseous permeation at high temperatures; they found higher solubilities in the base metal, while diffusivity differences were small. Due to this increasing research interest in hydrogen embrittlement behaviour of Cr-Mo steels, the properties of a 2.25Cr-1Mo steel – a material commonly present in boilers and pressure reactors that can suffer hydrogen damage – are considered here [33] in the simulated welded joints. Cr-Mo steels have been proposed as candidates for high-pressure gaseous hydrogen storage and transport [34,35]. However, the experimental scatter in trap densities and diffusivities due to the wide range of possible microstructures hinders a predictive numerical modelling; thus, a parametric study is performed here for the sake of generalisation.

The present research has the aim of studying hydrogen transport near a crack tip that is located in a welded joint. A graded material is reproduced by modelling weld and heat affected zone layers surrounded by the base material. Stress fields are simulated considering a Boundary Layer approach in which a remote load is applied whereas hydrogen diffusion and trapping are simultaneously solved using ABAQUS user subroutines. Constraint effects are briefly discussed but the focus is put on the assessment of trapping phenomena. The influence of non-homogeneous multi-trapping is investigated, and the numerical simulation of hydrogen entry is also discussed. The paper is organised as follows: Section 2 presents the Boundary Layer approach that models the welded joint; the considered layer configurations, loading conditions, geometry and mesh are also described. Mechanical properties of a 2.25Cr-1Mo steel are discussed within a weld modelling framework and the implemented stress–strain response is presented. Section 3 establishes the hydrogen transport model, comprising the trapping-modified governing equation and the stress-dependent boundary conditions. Diffusion properties and trapping characterisation of 2.25Cr-1Mo steels are also discussed and the simulated trapping parameters are defined. Finally, considering the previously delimited parametric study, results for the stress distributions and the obtained hydrogen concentrations are presented and discussed in Section 4.

2. Boundary layer approach

The boundary layer (BL) formulation to analyse the small scale yielding problem and to find stress fields near a crack tip was firstly developed by Rice (1968) [36]. Boundary Layer simulations have been used to study both ductile crack growth [37] and brittle fracture [38]. Constraint effects have been also extensively explored [39–41]. Detailed discussions on the representativity of Modified Boundary Layer (MBL) approaches in comparison to full-field models can be found in the work of Betegón and Peñuelas (2006) [42] and, regarding hydrogen-diffusion in pressure pipes, following Dadfarnia et al. (2008) [43]. In the present work, the influence of T constraint is not analysed and a Boundary Layer simplified approach, i.e. assuming a constraint parameter $T = 0$.

2.1. Geometry and loading

The chosen geometry follows the pioneering work of Sofronis and McMeeking (1989) [44]: the outer radius R is fixed to 150 mm whereas the initial crack opening is $b_0 = 0.010$ mm, so the crack tip radius is $b_0/2 = 0.005$ mm. The crack behaviour is modelled, as already mentioned, using a Boundary Layer approach, i.e. applying remote displacements in a far-field outer radius so the Liner Elastic Fracture Mechanics assumptions are valid. Being the x-axis and y-axis parallel and perpendicular to the crack plane, respectively, the following horizontal, u_x, and vertical, u_y, displacements are imposed at the outer radius, R:

$$u_x = K_I \frac{1+\nu}{E}\sqrt{\frac{R}{2\pi}}\,(3-4\nu-\cos\theta)\cos\left(\frac{\theta}{2}\right) \tag{1}$$

$$u_y = K_I \frac{1+\nu}{E}\sqrt{\frac{R}{2\pi}}\,(3-4\nu-\cos\theta)\sin\left(\frac{\theta}{2}\right) \tag{2}$$

where $E = 210$ GPa is the Young's modulus, $\nu = 0.3$ is the Poisson coefficient and θ the polar coordinate associated to each node on the outer boundary. Plane strain conditions have been assumed. The simulated stress intensity factor is $K_I = 89.1\ \mathrm{MPa}\sqrt{\mathrm{m}}$, which was also considered by Sofronis and McMeeking (1989) [44]; geometry and loading from that work have been reproduced in many works regarding hydrogen transport near a crack tip [45–49], so it can be regarded as a benchmark for diffusion modelling. For Boundary Layer studies, loading is also expressed in terms of elasto-plastic J integral; the following equivalence is then taken into account:

$$J = \frac{K_I^2\left(1-\nu^2\right)}{E} \tag{3}$$

The implemented load $K_I = 89.1\ \mathrm{MPa}\sqrt{\mathrm{m}}$, is equivalent to a $J = 34.4$ N/mm following this relationship; J is also used to scale the distance to the crack tip. A non-homogeneous Boundary Layer is modelled

by considering different layers parallel to the crack surface so three sections are assigned to the Finite Element simulation: weld metal (WM), a heat affected zone (HAZ) and the base metal (BM). In the present work, constraint effects are briefly reviewed since the focus is put on the effect of diffusion-related parameters on hydrogen redistribution near a crack in a welded joint, so the extensive discussion about mismatching effects is overlooked. Within this context, Betegón and Peñuelas (2006) [42] analysed different weld widths from 2 to 20 mm. Peñuelas et al. (2006) [37] also studied this range within a ductile failure modelling framework. Kumar et al. (2014) [50] studied weld-centred cracks and considered WM widths of 5 and 10 mm, finding that for the same normalised loading parameters and plastic interaction, the opening stresses are independent of weld width. Constraint and mismatch effects were studied by Burstow et al. (1998) [39], simulating weld semi-widths from 0.625 to 40 mm. This work also demonstrated the self-similarities of stress fields under the same normalised load $J/h\sigma_{0,w}$, where h was the WM semi-width and $\sigma_{0,w}$ the WM yield stress. On the other hand, XB Ren et al. [24,25] considered a circular weld or "spot weld" around the crack tip with a weld radius of 10, 15 or 20 mm.

In contrast to the cited literature, here a HAZ layer is also modelled in both weld sides with the aim of simulating hydrogen transport between regions and trapping interactions. The HAZ width can be estimated following Rosenthal theory and can vary between 2 and 10 mm depending on the heat input [51]. Moltubakk et al. (1999) [52] simulated a crack within a MBL geometry, varying its position from the WM layer to the coarse-grained HAZ (CG-HAZ). Simulations of a three-point bending test with a weld centre crack and different HAZ and weld widths were performed by Rodrigues et al. (2004) [53], analysing HAZ widths of 2, 5 and 8 mm and WM widths of 6, 8 and 10 mm. As shown in Table 1, widths from 2.5 to 5 mm for both WM (h_{WM}) and HAZ (h_{HAZ}) are defined for the simulations performed here to find the influence of weld regions of hydrogen accumulation. The denomination of each configuration shown in Table 1 is used to identify results in Section 4.

Crack is simulated both in the WM and in the HAZ. The setting of layers and the possible crack location within the Boundary Layer model can be seen in Fig. 1. It must be noted that the nomenclature h_{WM} and h_{HAZ} in this work refers to the layer width, in contrast to other literature where this variable accounts for the weld semi-width. The complete Boundary Layer is modelled because for the HAZ crack configuration, no symmetry can be assumed.

Stress–strain fields and hydrogen distributions are solved in the commercial software ABAQUS through an implicit scheme and for quadratic plane strain elements with reduced integration and the additional temperature degree of freedom. User subroutines are also employed in order to model all the combined effects. To apply the remote displacements expressed in (1) and (2), a DISP subroutine is used. Loading is incrementally applied during a transient step of 100 s and kept constant during a second steady state step. The choice of 100 s is arbitrary but follows the order of magnitude shown by other authors [44,45] in which steady state is not reached yet and trapping effects still affect transient redistribution. Implementation details for hydrogen diffusion and trapping modelling are discussed in Section 3. The boundary layer mesh is shown in detail in Fig. 2.

Table 1
Definition of each layer configuration considering that the crack is centred in the heat affected zone or in the weld metal; different widths for each layer are also assessed.

Layer configuration	Crack location	h_{WM} (mm)	h_{HAZ} (mm)	Denomination
#1	Weld metal	2.5	0	WM2.5
#2	Weld metal	5.0	2.5	WM5-HAZ2.5
#3	Weld metal	2.5	2.5	WM2.5-HAZ2.5
#4	Heat affected zone	2.5	2.5	HAZ2.5-WM2.5
#5	Heat affected zone	2.5	5.0	HAZ2.5-WM5

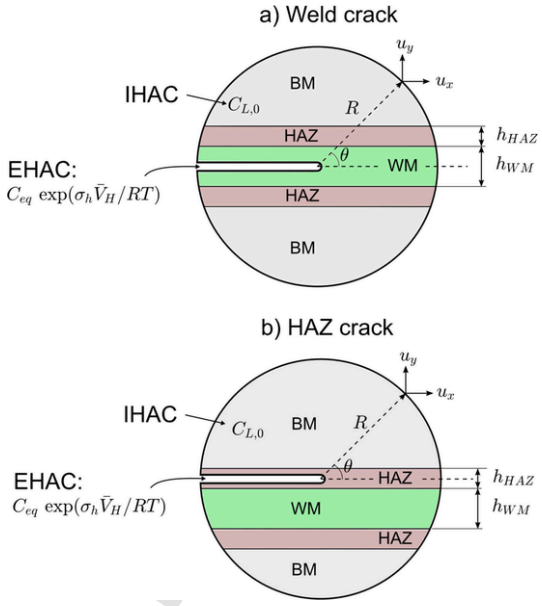

Fig. 1. Scheme of the performed simulations with two different crack locations, far-field imposed displacements and two hydrogen source cases: Environment Hydrogen Assisted Cracking (EHAC) and Internal Hydrogen Assisted Cracking (IHAC).

2.2. Mechanical properties

Heat affected zones can be very narrow and mechanical properties hard to obtain through a conventional tensile test; therefore, different approaches have been followed to identify typical tensile properties, e.g. correlation with miniature tests [33] or correlation with micro-hardness measurements [54]. It is also common to produce simulated HAZ specimens by subjecting the bulk material or specimens to a heat treatment and subsequent cooling that reproduce the thermal cycle of welding [29]. Even though the initial distribution of mechanical properties can be known, response to aging phenomena can be different between regions [55] so mismatching conditions can change during the service life. After the PWHT, in addition to residual stress relieving, a tempering effect is also expected for weldments [56]. Strength after welding will also depend on the heat input, as demonstrated by Prasad and Dwivedi et al. (2008) [57], and on the complete temperature history, bearing in mind the possible PWHT. High heat inputs produce microstructures with lower yield stress and ultimate strength whereas the % elongation is increased.

The simulated materials for each weld region are based on results found by Karthik et al. (2002) [33] for a 2.25Cr-1Mo steel. They used a correlation between shear punch test results and tensile properties in order to obtain the distribution along the HAZ, as shown in Fig. 3; however, only WM, HAZ and BM are simulated so the properties of sub-regions (Coarse-Grained, Fine-Grained and Inter-Critical HAZs) from [33] are averaged. As in [33], the hardening exponent n is determined considering the relationship between ultimate and yield stresses: $(n/0.002)^n = \sigma_u/\sigma_{ys}$.

The averaged yield stresses for the three regions WM, HAZ and BM, $\sigma_{0,w}>\sigma_{0,h}>\sigma_{0,b}$, respectively, lead to an overmatching situation. The hardening behaviour of each layer is assumed to follow a power-law

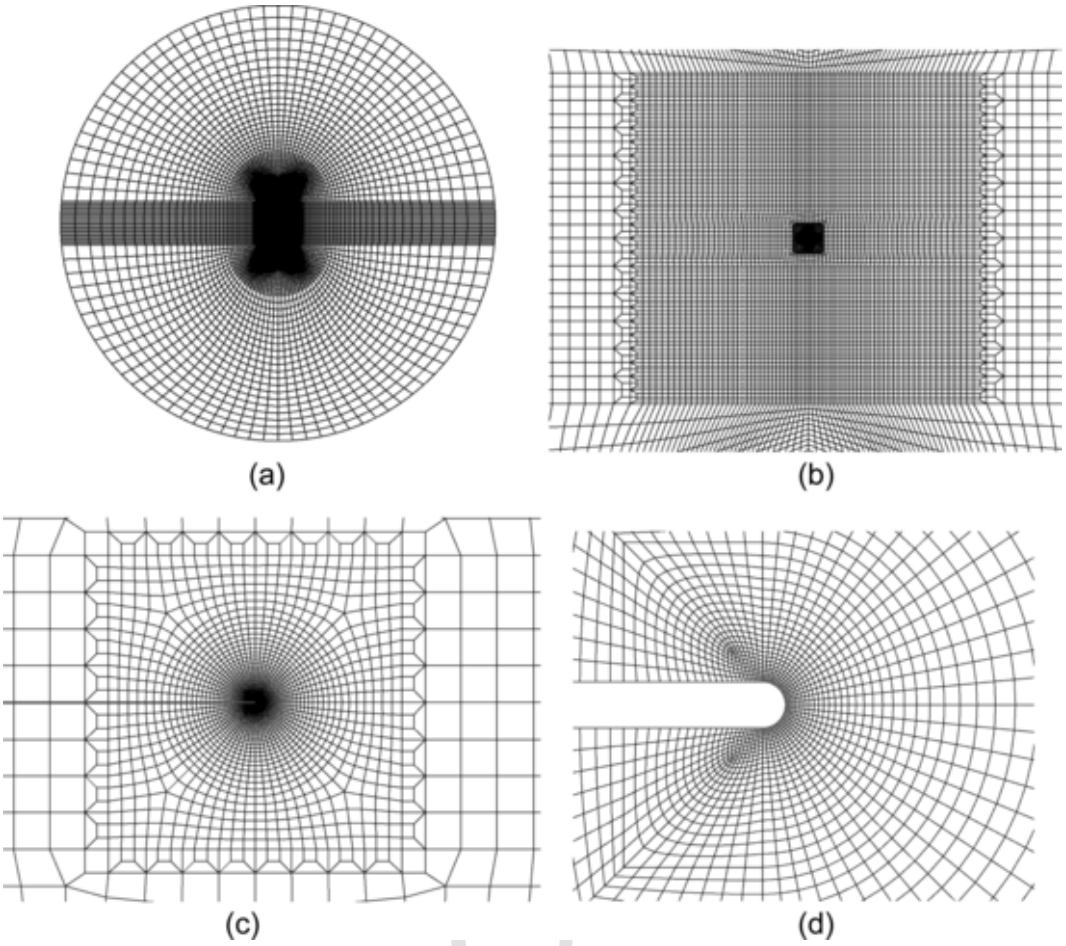

Fig. 2. Mesh of Boundary Layer: (a) complete model with 150-mm radius; (b) grid of 25-mm width to model layered weld and heat affected zones; (c) grid of 2.5-mm width; (d) crack tip meshing with an initial radius of $b_0/2 = 0.005$ mm.

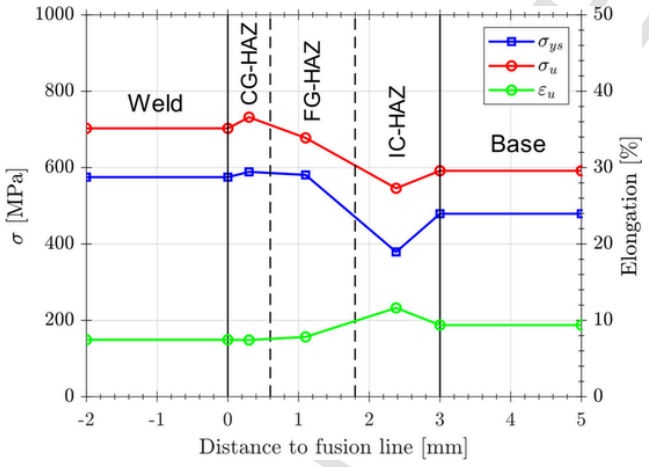

Fig. 3. Tensile properties along the regions of a 2.25Cr-1Mo steel weld obtained using a correlation with shear punch tests [33].

hardening:

$$\sigma_y = \sigma_0\left(1 + E\frac{\varepsilon^p}{\sigma_0}\right)^n \tag{4}$$

where the yield stress σ_0 and the hardening exponent n of each layer determine a stress–strain curve that is implemented in ABAQUS through the $\sigma_y(\varepsilon^p)$ function plotted in Fig. 4.

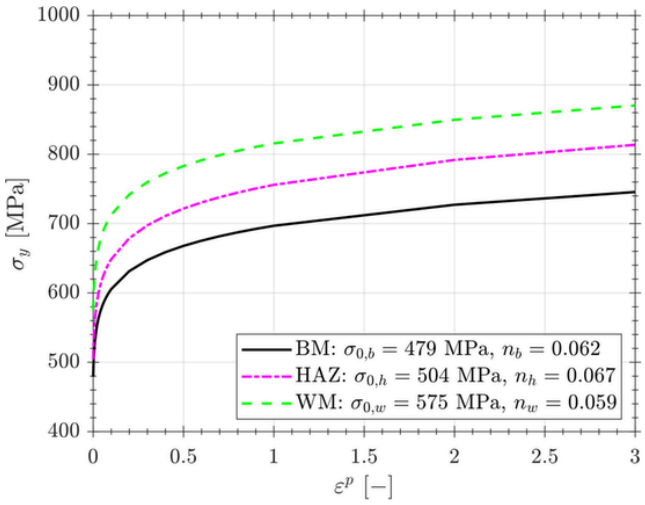

Fig. 4. Stress – plastic strain curves that have been implemented to model hardening behaviour of each layer.

Considering the fixed loading $J = 34.4$ N/mm and the simulated layer widths (h_{WM}, h_{HAZ}between 2.5 and 5 mm), and recalling that here h represents the semi-width to be compared with other works ($h_{WM}; h_{HAZ} \equiv 2h$), the normalised $h\sigma_{0,w}/J$ equals 16.72 to 83.6, which represents a relatively high value [42]. Additionally, overmatching ratios are low, $\sigma_{0,w}/\sigma_{0,h} = 1.14$ and $\sigma_{0,h}/\sigma_{0,b} = 1.05$, so reduction in con-

straint and important stress field modifications are not expected and the non-homogeneous stress distribution should be close to the homogeneous weld solution [39,42].

3. Hydrogen transport model

Modelling approaches for hydrogen transport are based on thermodynamic assumptions and the classical Fick's equation [2,44,58,59]. The conventional approach assumes only a modification of diffusivity and solubility depending on material microstructure. However, this approach is limited because effective diffusivity depends on concentration so it is a local variable and because it relies on analytical fitting methods that simplify real surface phenomena [60–62]. Thus, trapping influence is implemented by including a local concentration of hydrogen in traps, C_T, that is distinguished from the lattice hydrogen concentration, C_L.

3.1. Governing equations

Generalising the two-level approach to a multi-trapping equation, i.e. with various C_T^i, the mass balance is modified:

$$\frac{\partial C_L}{\partial t} + \sum_i \frac{\partial C_T^i}{\partial t} - \nabla\hat{A}\cdot\left(D_L\nabla C_L\right) + \nabla\hat{A}\cdot\left(\frac{D_L C_L \bar{V}_H}{RT}\nabla\sigma_h\right) = 0 \tag{5}$$

where D_L is the hydrogen diffusivity in ideal lattice, R the gas constant, T the temperature, and the last term including the partial molar volume, $\bar{V}_H$, and hydrostatic stress, σ_h, accounts for the stress-drifted diffusion and the decrease in chemical potential of lattice sites when they are subjected to tensile hydrostatic stresses [44,63,64]. The analogy between the mass balance equation (5) is exploited in a UMATHT ABAQUS subroutine so the C_L local variable is stored in the temperature degree of freedom. The hydrostatic stress gradient $\nabla\sigma_h$ is determined through a USDFLD subroutine, as detailed in [48].

Typically, the Oriani's equilibrium [65] is assumed so the trapping occupation, i.e. the ratio of hydrogen concentration over the density of trapping sites $\theta_T^i = C_T^i/N_T^i$, can be expressed as a function of C_L. Thus, the concentration of hydrogen in each defect type is:

$$C_T^i = \frac{N_T^i}{1 + \frac{N_L}{C_L \exp(E_B^i/RT)}} \tag{6}$$

where E_B^i is the binding energy associated to the corresponding trapping site and N_L is the density of lattice sites. This univocal relationship between trapping concentration C_T and lattice concentration C_L facilitates numerical implementation because the evolution of hydrogen in traps can be obtained once the dependent solution of the mass balance is known. In this work, as described in Section 3.3, two kind of traps are considered: microstructural traps independent of plastic strain (m superscript) and traps associated to the multiplication of dislocations due to plasticity (p superscript). The multi-trapping framework has been developed previously by other authors [59,66,67]. In order to rearrange the governing equation, the chain rule must be taken into account:

$$\frac{\partial C_L}{\partial t} = \frac{\partial C_T^m}{\partial C_L}\left(\frac{\partial C_L}{\partial t}\right) + \frac{\partial C_T^p}{\partial C_L}\left(\frac{\partial C_L}{\partial t}\right) + \frac{\partial C_T^p}{\partial N_T^p}\frac{dN_T^p}{d\varepsilon^p}\frac{\partial \varepsilon^p}{\partial t} \tag{7}$$

This expression (7) can be derived assuming thermodynamic equilibrium, as in (6). Deriving and substituting, as in Krom et al. (1999) [45], the equation that is implemented in a UMATHT subroutine can be expressed in the following terms:

$$\left(1 + \frac{C_T^m(1-\theta_T^m)}{C_L} + \frac{C_T^p(1-\theta_T^p)}{C_L}\right)\frac{\partial C_L}{\partial t} - \nabla\hat{A}\cdot\left(D_L\nabla C_L\right) + \nabla\hat{A}\cdot\left(\frac{D_L C_L \bar{V}_H}{RT}\nabla\sigma_h\right) + \theta_T^p\frac{dN_T^p}{d\varepsilon^p}\frac{\partial\varepsilon^p}{\partial t} = 0 \tag{8}$$

where the las term, which is a consequence of the chain rule and the plastic strain dependency of N_T^p, was firstly proposed by Krom et al. (1999) [45]. The influence of this term is strong for high loading rates since the fast creation of traps produces trap depletion [45,68,69].

3.2. Boundary conditions

The outer far-field boundary is assumed to be insulated for every simulation, i.e. zero-flux is assigned, whereas the crack surface is modelled considering two situations: (i) Environment Hydrogen Assisted Cracking (EHAC), in which hydrogen is continually generated on the crack surface and (ii) Internal Hydrogen Assisted Cracking (IHAC), where hydrogen pre-charging has taken place, e.g. during testing or in-service components, but the H source is not present during loading. Even though embrittlement mechanisms should be the same for both processes, the amount of hydrogen near the crack tip can be affected by the occurrence of EHAC or IHAC [70,71].

To model the IHAC after considering a predefined field $C_{L,0}$ as the initial condition, all boundaries, including the crack surface, are assumed to be insulated. The zero-concentration boundary condition is here not explored but it is highlighted the need of appropriate and generalised boundary conditions for hydrogen uptake and exit [72,73]. For EHAC, a stress-dependent concentration must be implemented, as shown by Di Leo et al. (2013) [47] in order to realistically reproduce hydrogen entry, because the constant magnitude in equilibrium is the chemical potential rather than the lattice concentration. This physical surface phenomenon is translated to the following boundary condition in terms of lattice concentration along the crack boundary $\mathscr{B}_c$:

$$C_L\left(\mathscr{B}_c\right) = C_{eq}\exp\left(\frac{\sigma_h(\mathscr{B}_c)\bar{V}_H}{RT}\right) \tag{9}$$

The implementation of this boundary condition is done through a DISP subroutine in ABAQUS, following the heat transfer analogy [48,74]. A URDFIL subroutine is also used to store hydrostatic stress σ_h values averaged at nodes.

3.3. Diffusion and trapping parameters

Diffusion properties that are related to lattice sites also follow the work of Sofronis and McMeeking (1989) [44], and are shown in Table 2.

With the aim of modelling the microstructure variation in a welded joint, two types of traps are considered. One kind of trap is included to simulate plastic distortion (N_T^p, E_B^p), i.e. modelling trapping in dislocations. N_T^p density is implemented as a function of dislocation density ρ,

Table 2
Diffusion parameters considered in all simulations.

D_L	1.27×10^{-8} m^2/s
N_L	5.1×10^{29} sites/m^3
$\bar{V}_H$	2.0×10^{-6} m^3/mol
T	293 K
$C_{L,0} = C_{eq}$	2.1×10^{21} atoms/m^3

which is dependent on equivalent plastic strain ε^p. A geometric relationship between dislocation density and N_T^p is assumed [67]:

$$N_T^p = \frac{\sqrt{2}\rho}{d} \tag{10}$$

where the lattice parameter d is taken as 2.87×10^{-10} m, and the dislocation density ρ is assumed as [67]:

$$\rho = \begin{cases} \rho_0 + 2\gamma\varepsilon^p, \varepsilon^p < 0.5 \\ \rho_0 + \gamma, \varepsilon^p \geq 0.5 \end{cases} \tag{11}$$

The dislocation density in the unstrained material ρ_0 is taken as 10^{10} line length/m^2 and the parameter $\gamma = 10^{16}$ line length/m^2 [66]. This modelling approach based on dislocation density facilitates the incorporation of mechanistic Strain Gradient Plasticity theories [49]; in that case, the role of Geometrically Necessary Dislocations in trapping phenomena should be better understood. On the other hand, a kind of trap accounting for microstructure (N_T^m, E_B^m) is also modelled. This includes grain boundaries, or lath boundaries in martensitic microstructures, and precipitates, e.g. carbides. N_T^mdensity is assumed to take different values for each weld region but independent of stress or plastic deformation. For the choice of N_T^m and E_B^m, D_{app} from literature can be analysed. However, as shown by Raina et al. (2017) [75], in order to fit both parameters, trap density and binding energy, permeation tests need to be performed covering various trapping ranges. Other option is to find E_B^m through TDS measurements and to fit N_T^m from permeation transients by assuming diluted or saturated limiting cases [58,76].

Peral et al. (2020) [77] studied trapping densities for water-quenched 2.25Cr-1Mo and 2.25Cr-1MoV, using electropermeation tests and finding N_T values between 1.1×10^{24} and 4.2×10^{26} traps/m^3, depending on the tempering temperature and the V-addition. They also measured detrapping energies in TDS tests and found three types of defects for some heat treatments. Considering this variation in experimental results, the parameters shown in Table 3 are chosen to model a two-type trapping phenomenon. Without experimental testing, a multiplier φ is defined to perform a parametric study covering the range between 10^{24} and 10^{26} traps/m^3 [77]

In order to assess trapping effects, especially deep trapping, two materials are defined: (i) Material A with $\varphi_h = 1$, and $\varphi_w = 10$; (ii) Material B with $\varphi_h = 10$, and $\varphi_w = 100$. A summary of the parameter assignment for each layer, and the common elastic and hydrogen-related common parameters, can be seen in Fig. 5. The effect of PWHT on the defect reduction is not taken into account explicitly, but different ratios φ are assessed. Softening or hydrogen-enhanced dilatation are also neglected.

4. Results

4.1. Influence of weld and heat affected zone widths

The layer width can affect hydrogen transport in two ways: (i) modifying stress–strain fields or (ii) introducing secondary source and sink effects. The stress–strain influence is explained by the trapping-modified governing equation that includes the hydrostatic stress gradient and a trap density dependent on ε^p. Even though a high constraint

Table 3
Parameters modelling trapping effect for plastic-related dislocations (^{p} superscript) and for the rest of microstructural defects (^{m} superscript).

	Trap density	Binding energy
Base Metal	$N_{T,b}^m$ =1.0×10 ^{24} m $^{-3}$	$E_{B,b}^m$ =30 kJ/mol
Heat Affected Zone	$N_{T,h}^m = \varphi_h N_{T,b}^m$	$E_{B,h}^m$ =40 kJ/mol
Weld Metal	$N_{T,w}^m = \varphi_w N_{T,b}^m$	$E_{B,w}^m$ =40 kJ/mol
All regions	$N_T^p(\varepsilon^p)$	E_B^p =20 kJ/mol

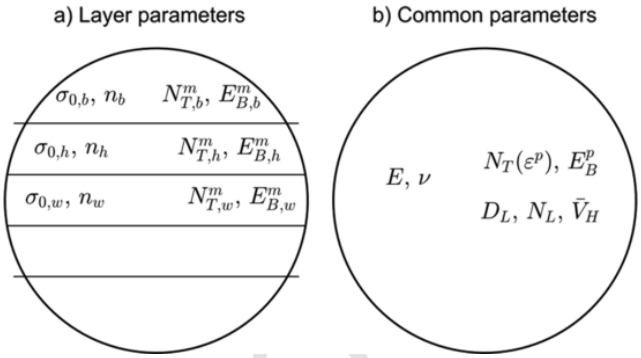

Fig. 5. Definition of (a) layer-dependent properties and (b) common parameters for all weld regions.

effect is expected due to the high $h\sigma_0/J$ value, the opening stress (σ_{22}) is plotted in Fig. 6 for all the studied configuration. It must be recalled that the results for HAZ2.5-WM2.5 and HAZ2.5-WM5 correspond to a crack located in the heat affected zone so complete symmetry does not occur: an undermatching effect on the BM side takes places ($\sigma_{0,h}>\sigma_{0,b}$) while on the opposite Boundary Layer surface an overmatching constraint happens ($\sigma_{0,h}<\sigma_{0,w}$). In order to facilitate generalisation, all axes are normalised: each stress curve is scaled by the corresponding σ_0 of the centre layer and the non-dimensional distance to the crack tip is plotted as $r\sigma_0/J$.

As shown in Fig. 6, opening stress peaks are located between $r\sigma_0/J = 1.75$ and 2.0; this normalised distance is equivalent, for the considered materials and loads, to a $r \approx 0.10$ mm. Stress distributions are plotted for the loading level $K_I = 89.1$ MPa$\sqrt{\text{m}}$, reached at the end of the transient first step of 100 s. For the sake of comparison, all plots correspond to the plane parallel to the crack, i.e. for $\theta = 0$; nevertheless, it must be noted that for non-symmetric situations in which the crack is centred in the HAZ layer, a slight deviation from symmetric propagation could occur. A small increase in σ_{22} is found when the crack is located within the heat affected zone indicating a higher constraint level. This result is explained by the fact that the heat affected region lies between a softer layer and a harder layer, so undermatching/overmatching effects are simultaneously taking place, whereas for the weld-centred crack, overmatch dominates. For the three configurations simulating a weld-centred crack, σ_{22} is higher for the WM5-HAZ2.5 so it is concluded that a thick weld joint is more constrained than a thin weld. The opening stress σ_{22} contours in MPa for the config-

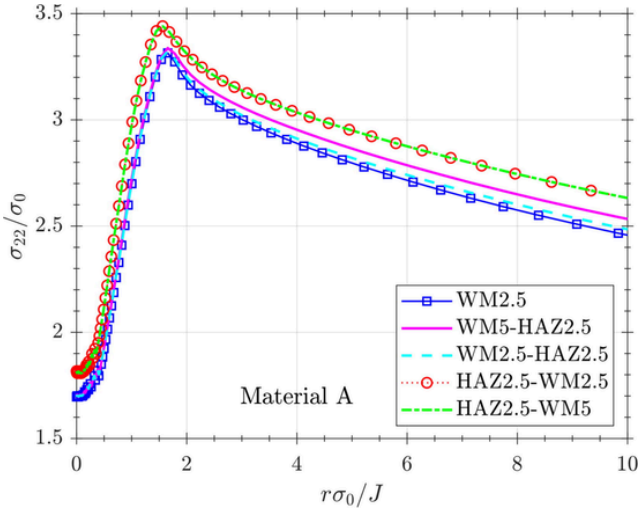

Fig. 6. Normalised opening stress for different welding/crack configurations and Material A.

uration WM2.5-HAZ2.5 are shown in Fig. 7. For all simulations, geometrical non-linearities, i.e. finite deformations, have been considered due to the highly deformed crack tip.

Nevertheless, the magnitude driving diffusion is the hydrostatic stress σ_h that is plotted in Fig. 8 for the considered configurations. Maximum hydrostatic stress lies slightly closer, $r\sigma_0/J = 1.5$ to 1.7, to the crack tip in comparison to the opening stress. Due to this stress tendency, after 100 s of diffusion hydrogen in lattice sites accumulates near a local peak at $r\sigma_0/J = 1.25$ to 1.5, which is closer than the maximum σ_h, indicating that steady state values have not been reached yet. As previously mentioned, the present diffusion modelling framework is capable of including the role of dislocations in trapping and might be combined with advanced plasticity theories, e.g. Strain Gradient Plasticity. It is worth considering that these theories predict a significant stress raise in the vicinity of the crack tip [78], so the results here presented are valid only for classic J2 plasticity assumptions. The differences between steady state and 100 s concentrations are discussed in Section 4.3. Fig. 9 shows concentrations of diffusible hydrogen, which is defined as the sum of C_L and C_T^p, i.e. hydrogen in lattice sites and hydrogen weakly retained in dislocations. Hydrogen transport by mobile dislocations is not considered, but it can affect local diffusion

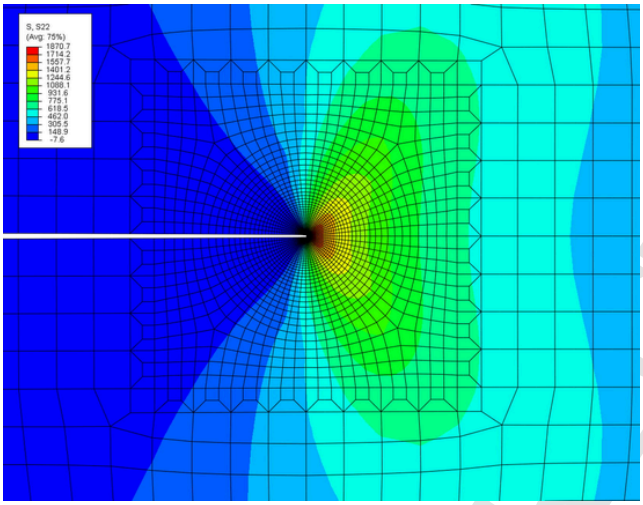

Fig. 7. σ_{22} for WM2.5-HAZ2.5 and Material A.

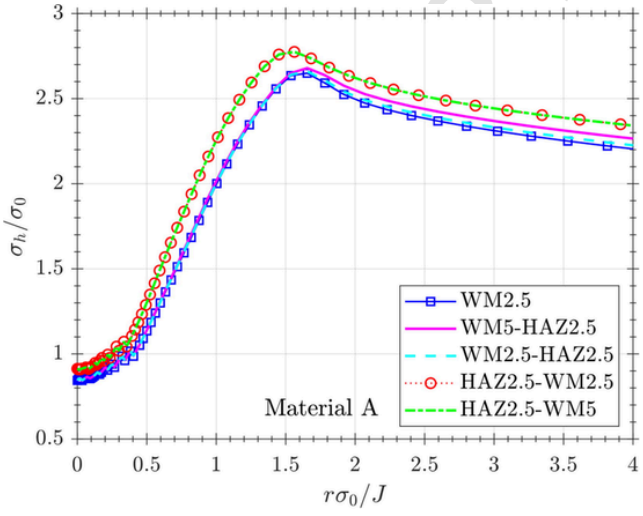

Fig. 8. Normalised hydrostatic stress for different welding/crack configurations and Material A.

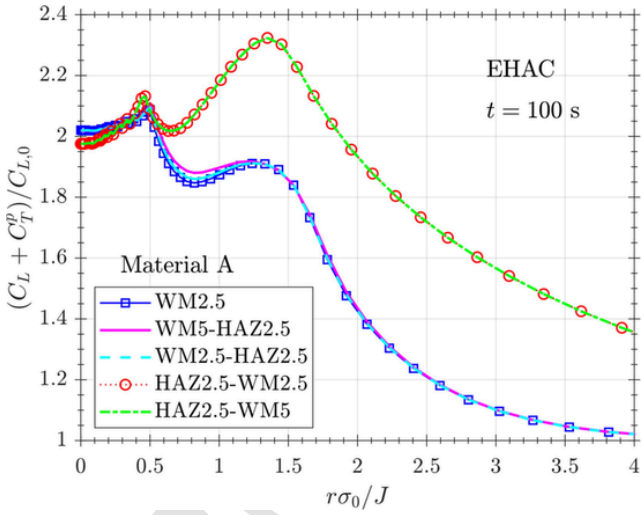

Fig. 9. Normalised diffusible hydrogen for different welding/crack configurations considering hydrogen uptake from the crack surface (EHAC) and Material A.

[67]. Results for all weld configurations display a secondary peak closer to the crack tip, at $r\sigma_0/J \approx 0.5$, that is associated to the maximum synergy between the increase in $N_T^p(\varepsilon^p)$ due to plastic deformation and the hydrostatic stress raise. Fig. 9 assumes a continuous hydrogen source from the crack tip, reproducing EHAC conditions; thus, stress dependency of concentrations is also being simulated in the crack tip $r\sigma_0/J = 0$.

4.2. Modified material constraint

Even though the focus is put on the mechanical properties extracted from [33] for a real 2.25Cr-1Mo weld, other mismatching ratios are simulated with the aim of extending the conclusions to other situations. Constraint is artificially modified by increasing overmatching and defining other two materials: (i) Material C with a 50% reduction in the yield stress of the heat affected zone, $\sigma_{0,h}$, and a base material $\sigma_{0,b}$ divided by 3; (ii) Material D with yield stresses of all regions uniformly reduced to the 50%. Material C implies the same $h\sigma_{0,w}/J$ than Material A but with different mismatching ratio m. On the other hand, Material D considers a reduction of 50% in $h\sigma_{0,w}/J$ but the same mismatching ratio than Material A. Even though material properties have been artificially modified, Material C and Material D could represent limiting cases, respectively, of strong gradients in mechanical properties due to a fast cooling process after welding or a uniformly softened joint due to a post-weld heat treatment. These two trivial materials have the same diffusion and trapping-related properties than Material A so only stress–strain effects are operating on hydrogen transport differences.

Hydrostatic stress curves are shown in Fig. 10. Material C results in a similar hydrostatic stress distribution up to the distance $r\sigma_{0,w}/J = 2$ in comparison to Material A, but deviates from this behaviour at higher distances. Due to the artificially reduced constraint by a softer $\sigma_{0,h}$ and $\sigma_{0,b}$, i.e. a higher overmatch ratio, lower stresses were expected. Fig. 11 shows the σ_h contours in MPa (stored as State Variable SDV1 in the UMATHT subroutine); stress gradients produced by mismatch can be appreciated in the interface between WM and HAZ layers. In contrast, analysing the Material D curve, it is concluded that a uniform softening, shifts the σ_h peak towards the crack tip and increases its value. This softening, as shown in Fig. 12, produces a higher amount of diffusible hydrogen near the crack tip, which is explained by the ε^p increase and the consequent multiplication of dislocations that is equivalent to a high trap density N_T^p.

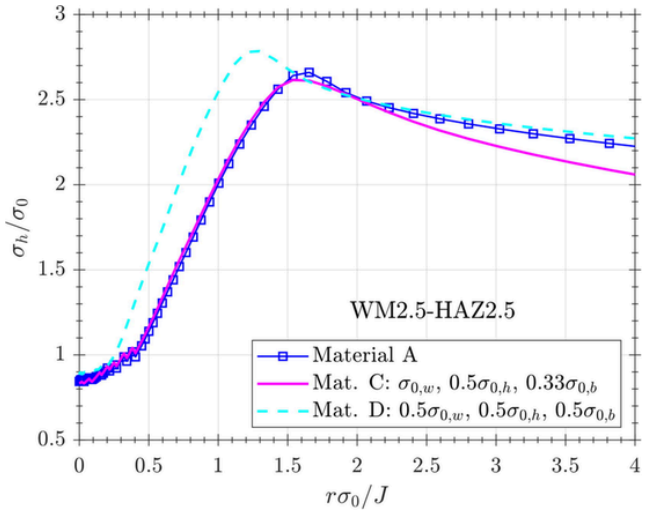

Fig. 10. Normalised hydrostatic stress for different mismatch ratios and for a crack in the weld material and widths $h_{WM} = h_{HAZ} = 2.5$ mm.

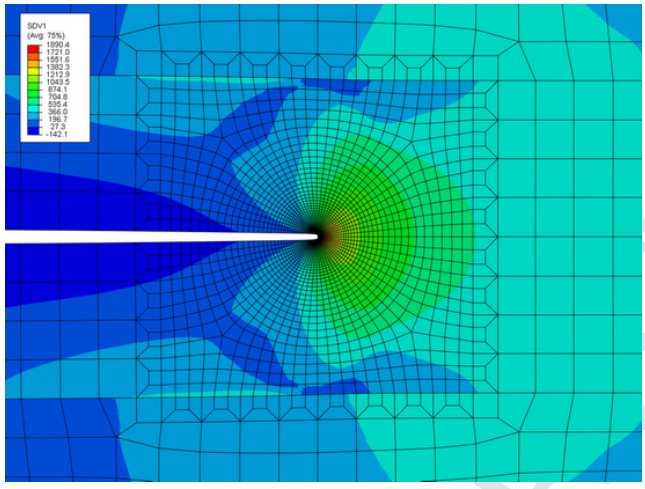

Fig. 11. σ_h for WM2.5-HAZ2.5 and Material C.

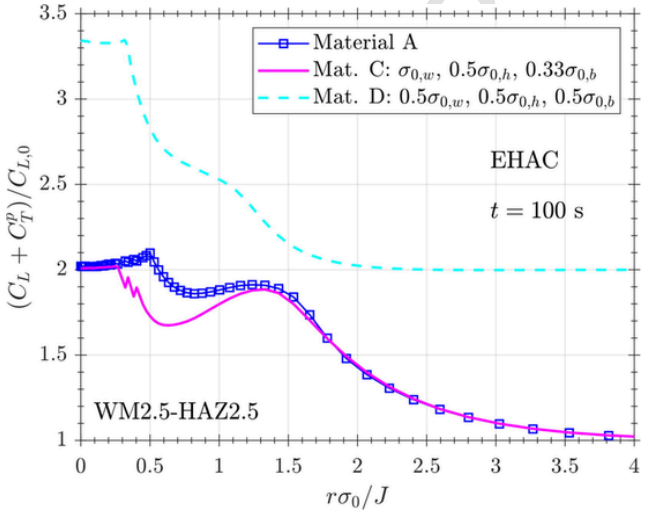

Fig. 12. Normalised concentration of diffusible hydrogen for different mismatch ratios and for a crack in the weld material and widths $h_{WM} = h_{HAZ} = 2.5$ mm.

4.3. Influence of trapping parameters and hydrogen source

Assuming that hydrogen moves towards tensile regions, after long diffusion times hydrogen distribution in lattice sites should follow the same tendency than hydrostatic stress. Plotting C_L for the configuration WM5-HAZ2.5 (Fig. 13), it is concluded that after 100 s, when the maximum load is reached, the equilibrium concentration has not still been reached. The difference between C_L at $t = 100$ s and steady state is higher than expected for the diffusion parameters mimicking the works of Sofronis and McMeeking (1989) and Krom et al. (1999) [44,45]. This can be explained by the different stress magnitude since lower σ_0 values were simulated in [44,45] and by the multi-trapping parameters considered here.

The influence of charging conditions is also assessed, finding that the stress-dependent boundary concentrations, which accurately reproduce EHAC for a loaded crack, result in a significant increase in hydrogen concentration in lattice sites in comparison with the insulated crack surface (IHAC). As already mentioned, zero-concentration boundary conditions are not analysed; that situation would surely promote lower concentrations near the crack tip and a complete depleted Boundary Layer at steady state.

Hydrogen distributions are also determined for Material B with $\varphi_h = 10$, and $\varphi_w = 100$ that reproduces a higher trapping density of microstructural defects in the HAZ ($N^m_{T,h} = \varphi_h N^m_{T,b}$) and in the WM ($N^m_{T,w} = \varphi_w N^m_{T,b}$), with respect to Material A ($\varphi_h = 1$, and $\varphi_w = 10$). Results for C_L (Fig. 14) show that a high trap density of defects delays the filling process of lattice sites even though the considered multiplied defects are independent on plastic strain. This delay should not be confused with the depletion predicted by Krom et al. (1999) [45] due to the fast creation of traps at high loading rates and modelled by the corresponding term in the mass balance.

With the aim of quantifying this delaying effect of microstructural traps, that have been modelled with a binding energy of $E^m_B = 40$ kJ/mol, an effective diffusivity is defined from the mass balance in equation (8) through the relationship with D_L:

$$\frac{D_L}{D_{eff}} = 1 + \frac{C^m_T(1-\theta^m_T)}{C_L} + \frac{C^p_T(1-\theta^p_T)}{C_L} \tag{12}$$

This term is a local magnitude that equals 1 for full traps ($\theta^m_T = \theta^p_T = 1$), but can take very high values when the concentration in

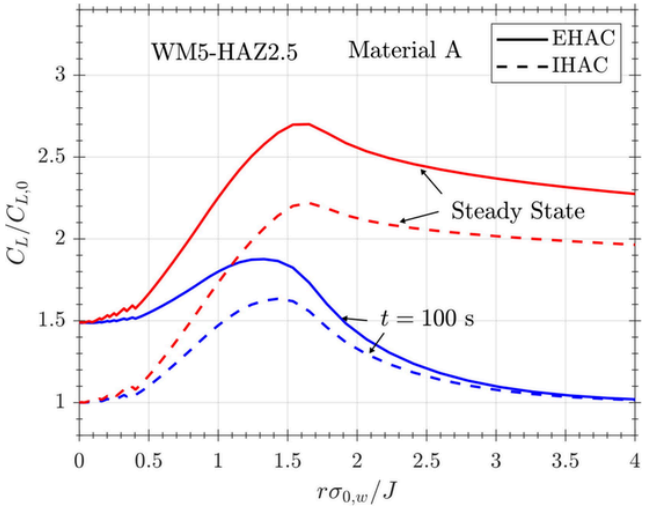

Fig. 13. Normalised concentration of hydrogen in lattice sites at 100 s and steady state for the configuration WM5-HAZ2.5 and trapping parameters of Material A. Comparison between EHAC and IHAC boundary conditions.

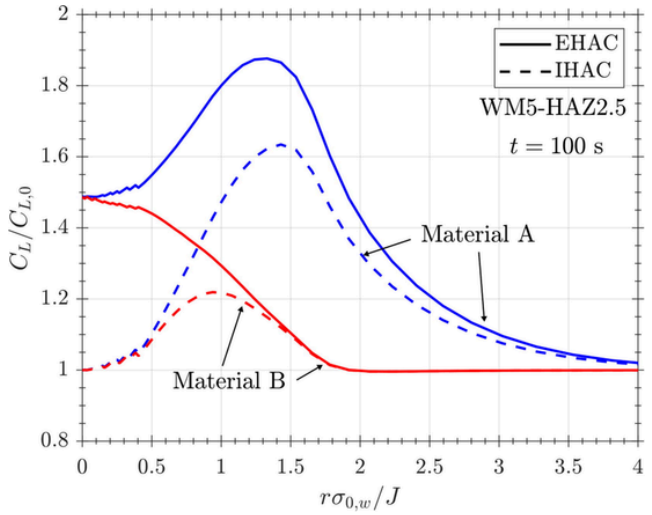

Fig. 14. Normalised concentration of hydrogen in lattice sites at 100 s for the configuration WM5-HAZ2.5. Comparison between Material A and Material B.

trapping sites is much higher than C_L even though trap occupancy is still low. In that case, the effective diffusivity D_{eff} is reduced and hydrogen transport is slower through the crack front. The inverse of equation (12), i.e. D_{eff}/D_L, is plotted in Fig. 15 for the IHAC boundary conditions at 100 s. It can be seen that for Material B, due to the high value of N_T^m, the conditions defined previously are verified: C_T^m is much higher than C_L but the trap occupancy θ_T^m is still low. Thus, D_{eff} decreases an order of magnitude for Material B in comparison to Material A. Similarly, since for both materials it is assumed a higher defect concentration N_T^m for the weld metal than for the heat affected zone ($\varphi_w = 10\varphi_h$), effective diffusivity is lower for the weld-centred crack.

Plotting in Figs. 16 and 17 diffusible concentrations ($C_L + C_T^p$) and hydrogen in microstructural defects (C_T^m), it is observed that C_T^m is much higher than diffusible hydrogen even for Material A, which has lower N_T^m than Material B. Concentration C_T^m also show a peak near $r\sigma_0/J = 1.5$, caused by the hydrostatic stress distribution. Concentrations are plotted in logarithmic scale to facilitate comparison. This difference between deeply trapped and diffusible hydrogen is lower for the crack located in the heat affected zone (Fig. 17) due to the assumed lower defect density N_T^m.

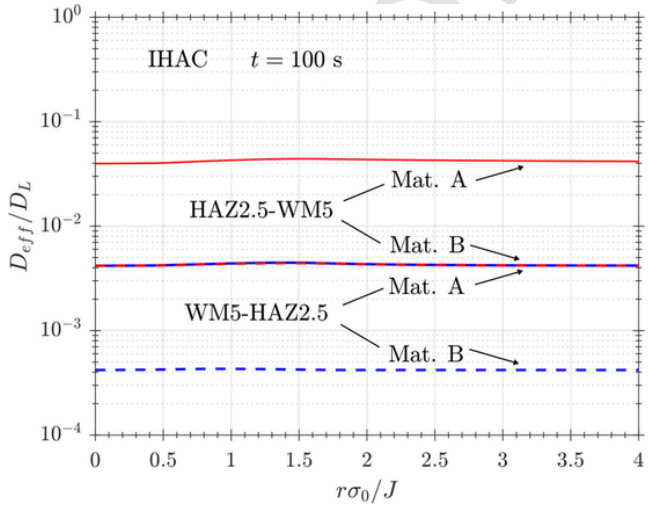

Fig. 15. Normalised effective diffusivity at 100 s for IHAC. Comparison between Material A and Material B and between WM5-HAZ2.5 and HAZ2.5-WM5.

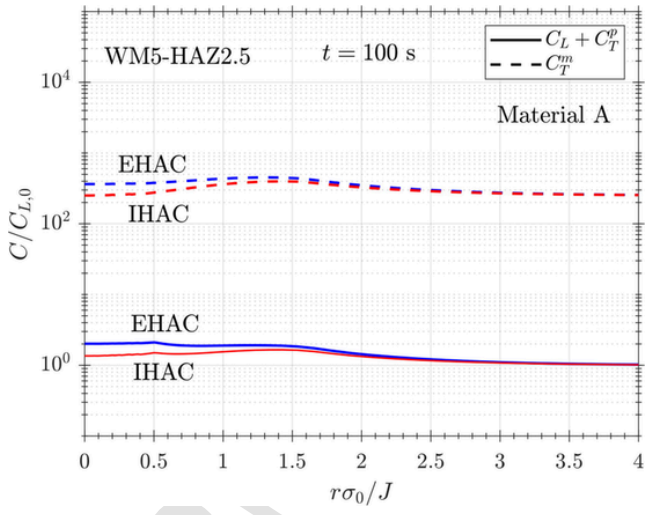

Fig. 16. Normalised hydrogen concentrations at 100 s for WM5-HAZ2.5. Comparison between diffusible and deeply trapped hydrogen.

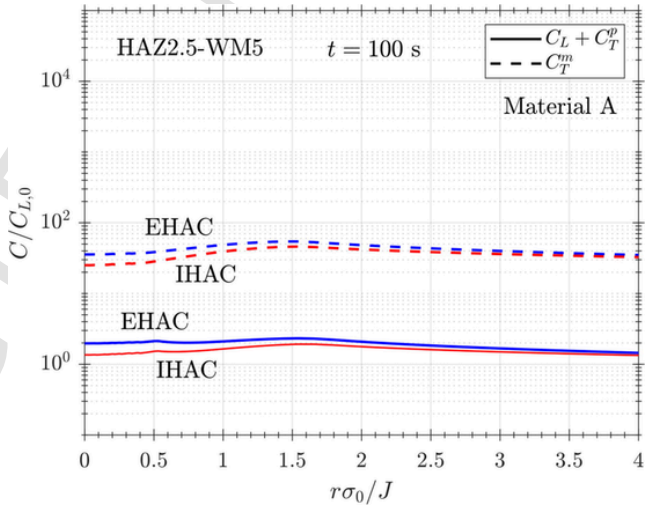

Fig. 17. Normalised hydrogen concentrations at 100 s for HAZ2.5-WM5. Comparison between diffusible and deeply trapped hydrogen.

The different trapping behaviour of HAZ and WM layers can be seen in C_T^m contours in Fig. 18.b for the configuration WM2.5-HAZ2.5. the TEMP contours that are plotted in Fig. 18.a represent C_L because the analogy between heat transfer and diffusion has been exploited through the UMATHT subroutine; it is demonstrated how hydrogen concentrates at lattice sites near the crack tip (Fig. 18.a).

The implications of these results for embrittlement are crucial; despite its lower value, the role of diffusible hydrogen ($C_L + C_T^p$) in damage micro-mechanisms can be important because its higher mobility. Whether stronger traps act as hydrogen sources or sinks during crack nucleation and propagation also needs to be elucidated for each specific case, depending on the trapping features and on the loading rates. It must be noted that the classification of hydrogen as diffusible or non-diffusible is relatively arbitrary because the experimental characterisation of traps is still controversial and even deeply trapped hydrogen can diffuse.

5. Conclusions

Hydrogen simulation near a crack tip in a welded joint has been numerically studied considering a Boundary Layer approach to model stress–strain fields. Additionally, a robust numerical framework for hydrogen multi-trapping modelling has been presented and implemented

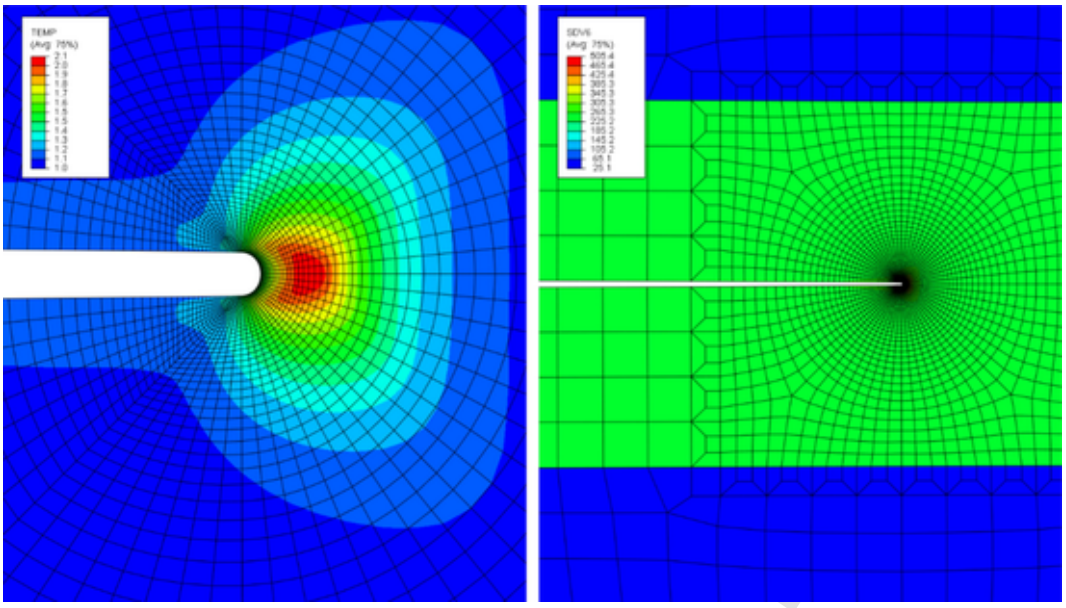

Fig. 18. Concentrations contours of: (a) hydrogen in lattice sites, $C_L/C_{L,0}$ and (b) deeply trapped hydrogen $C_T^m/C_{L,0}$. Results at 100 s for WM2.5-HAZ2.5, Material A and EHAC.

in ABAQUS through user subroutines. The following conclusions can be summarised:

- The influence of weld and heat affected zone widths is low for the simulated range. Due to the relatively low mismatching ratio and to the loading level, the stress field deviation from the homogeneous solution is slight. Thus, only small differences in lattice hydrogen are obtained for different widths.
- When mismatch or softening are enhanced by simulating artificial materials, constraint effects need to be considered and stress distributions affect the diffusion of hydrogen.
- Despite the small width influence, hydrogen transport is strongly affected by the crack location because different trapping parameters are assumed for the weld and for the heat affected zone.
- The experimental scatter in trapping densities and binding energies hinders the prediction of hydrogen trapping phenomena. However, it is demonstrated that two different effects can be simulated simultaneously to distinguish between diffusible and deeply trapped hydrogen.
- Two local peaks for diffusible hydrogen can be found when weak trapping is considered in dislocations that depend on plastic strain. A first peak, promoted by the plastic strain accumulation at the crack tip, is followed by the second peak in lattice hydrogen due to the hydrostatic stress maximum.
- The influence of a secondary trap type, which is independent of plastic strain and is here denominated as “microstructural” trapping, produces high trapped hydrogen concentrations but also a delay in hydrogen transport towards lattice and dislocation sites.
- The environment hydrogen assisted cracking conditions, as expected, produce higher concentration for both trapped and lattice hydrogen than the insulated boundary conditions. EHAC modelling requires the implementation of stress-dependent boundary conditions in order to accurately reproduce hydrogen entry.

In future research, residual stress and phase transformation produced by welding will be considered in a coupled thermo-mechanical simulation including temperature-dependent properties. Grain size effects will also be simulated in detail within the HAZ in order to capture accurate trapping behaviour of different regions (CG, FG and IC), and numerical models will be fed with experimental tests characterising traps. Additionally, a continuum model will be proposed so mechanical and diffusion-related properties progressively vary along the distance to the weld.

Declaration of Competing Interest

The authors declare that they have no known competing financial interests or personal relationships that could have appeared to influence the work reported in this paper.

Acknowledgements

The authors gratefully acknowledge financial support from the Ministry of Science, Innovation and Universities of Spain through gran RTI2018-096070-B-C33.

References

[1] E.A. Steigerwald, F.W. Schaller, A.R. Troiano, The role of stress in hydrogen induced delayed failure, J. Name Trans. Met. Soc. AIME; J. Vol. Vol 218; Other Inf. Orig. Receipt Date 31-DEC-61. (1960) Medium: X; Size: Pages: 832-41.
[2] R.A. Oriani, P.H. Josephic, Equilibrium aspects of hydrogen-induced cracking of steels, Acta Metall. 22 (1974) 1065–1074, doi:10.1016/0001-6160(74)90061-3.
[3] W.W. Gerberich, Y.T. Chen, Hydrogen-controlled cracking—An approach to threshold stress intensity, Metall. Trans. A. 6 (1975) 271–278, doi:10.1007/BF02667281.
[4] H.K. Birnbaum, P. Sofronis, Hydrogen-enhanced localized plasticity—a mechanism for hydrogen-related fracture, Mater. Sci. Eng. A. 176 (1994) 191–202, doi:10.1016/0921-5093(94)90975-X.
[5] J. Lufrano, P. Sofronis, H.K. Birnbaum, Modeling of hydrogen transport and elastically accommodated hydride formation near a crack tip, J. Mech. Phys. Solids. 44 (1996) 179–205, doi:10.1016/0022-5096(95)00075-5.
[6] J. Lufrano, P. Sofronis, H.K. Birnbaum, Elastoplastically accommodated hydride formation and embrittlement, J. Mech. Phys. Solids. 46 (1998) 1497–1520, doi:10.1016/S0022-5096(98)00054-4.
[7] O. Barrera, D. Bombac, Y. Chen, T.D. Daff, E. Galindo-Nava, P. Gong, D. Haley, R. Horton, I. Katzarov, J.R. Kermode, C. Liverani, M. Stopher, F. Sweeney, Understanding and mitigating hydrogen embrittlement of steels: a review of experimental, modelling and design progress from atomistic to continuum, J. Mater. Sci. 53 (2018) 6251–6290, doi:10.1007/s10853-017-1978-5.
[8] A. Turnbull, Modelling of environment assisted cracking, Corros. Sci. 34 (1993) 921–960, doi:10.1016/0010-938X(93)90072-O.
[9] J. Hirth, Effects of hydrogen on the properties of iron and steel, Metall. Trans. A. 11 (1980) 861–890, doi:10.1007/BF02654700.
[10] K. Hirata, S. Iikubo, M. Koyama, K. Tsuzaki, H. Ohtani, First-Principles Study on Hydrogen Diffusivity in BCC, FCC, and HCP Iron, Metall. Mater. Trans. A. 49 (2018) 5015–5022, doi:10.1007/s11661-018-4815-9.

[11] G.T. Park, S.U. Koh, H.G. Jung, K.Y. Kim, Effect of microstructure on the hydrogen trapping efficiency and hydrogen induced cracking of linepipe steel, Corros. Sci. 50 (2008) 1865–1871, doi:10.1016/j.corsci.2008.03.007.

[12] A. Oudriss, J. Creus, J. Bouhattate, C. Savall, B. Peraudeau, X. Feaugas, The diffusion and trapping of hydrogen along the grain boundaries in polycrystalline nickel, Scr. Mater. 66 (2012) 37–40, doi:10.1016/j.scriptamat.2011.09.036.

[13] A. Oudriss, J. Creus, J. Bouhattate, E. Conforto, C. Berziou, C. Savall, X. Feaugas, Grain size and grain-boundary effects on diffusion and trapping of hydrogen in pure nickel, Acta Mater. 60 (2012) 6814–6828, doi:10.1016/j.actamat.2012.09.004.

[14] R.M. Miranda, M.A. Fortes, Austenite grain growth, microstructure and hardness in the heat-affected zone of a 2.25 Cr-1Mo steel, Mater. Sci. Eng. A. 108 (1989) 1–8. doi:10.1016/0921-5093(89)90399-7.

[15] D. Deng, H. Murakawa, Finite element analysis of temperature field, microstructure and residual stress in multi-pass butt-welded 2.25Cr-1Mo steel pipes, Comput. Mater. Sci. 43 (2008) 681–695. doi:10.1016/j.commatsci.2008.01.025.

[16] B.A. Latella, S.R. Humphries, Young's modulus of a 2.25Cr-1Mo steel at elevated temperature, Scr. Mater. 51 (2004) 635–639. doi:10.1016/j.scriptamat.2004.06.028.

[17] C. Girish Shastry, P. Parameswaran, M.D. Mathew, K. Bhanu Sankara Rao, S.L. Mannan, The effect of strain rate and temperature on the elevated temperature tensile flow behavior of service-exposed 2.25Cr-1Mo steel, Mater. Sci. Eng. A. 465 (2007) 109–115. doi:10.1016/j.msea.2007.02.052.

[18] Properties and Selection, Irons, Steels, and High-Performance Alloys, ASM International (2018), doi:10.31399/asm.hb.v01.9781627081610.

[19] D. Deng, Y. Tong, N. Ma, H. Murakawa, Prediction of the residual welding stress in 2.25Cr-1Mo steel by taking into account the effect of the solid-state phase transformations, Acta Metall. Sin. (English Lett. 26 (2013) 333–339. doi:10.1007/s40195-012-0163-8.

[20] C. Heinze, C. Schwenk, M. Rethmeier, Numerical calculation of residual stress development of multi-pass gas metal arc welding, J. Constr. Steel Res. 72 (2012) 12–19, doi:10.1016/j.jcsr.2011.08.011.

[21] S.K. Bate, R. Charles, A. Warren, Finite element analysis of a single bead-on-plate specimen using SYSWELD, Int. J. Press. Vessel. Pip. 86 (2009) 73–78, doi:10.1016/j.ijpvp.2008.11.006.

[22] T.L. Panontin, M.R. Hill, The effect of residual stresses on brittle and ductile fracture initiation predicted by micromechanical models, Int. J. Fract. 82 (1996) 317–333, doi:10.1007/bf00013236.

[23] X. Qian, T. Li, Effect of residual stresses on the linear-elastic KI-T field for circumferential surface flaws in pipes, Eng. Fract. Mech. 77 (2010) 2682–2697, doi:10.1016/j.engfracmech.2010.06.014.

[24] X.B. Ren, Z.L. Zhang, B. Nyhus, Effect of residual stresses on the crack-tip constraint in a modified boundary layer model, Int. J. Solids Struct. 46 (2009) 2629–2641, doi:10.1016/j.ijsolstr.2009.02.009.

[25] X.B. Ren, Z.L. Zhang, B. Nyhus, Effect of residual stresses on ductile crack growth resistance, Eng. Fract. Mech. 77 (2010) 1325–1337, doi:10.1016/j.engfracmech.2010.03.007.

[26] X.B. Ren, Z.L. Zhang, B. Nyhus, Effect of residual stress on cleavage fracture toughness by using cohesive zone model, Fatigue Fract. Eng. Mater. Struct. 34 (2011) 592–603, doi:10.1111/j.1460-2695.2011.01550.x.

[27] W. Wu, Z. Liu, X. Li, C. Du, Z. Cui, Influence of different heat-affected zone microstructures on the stress corrosion behavior and mechanism of high-strength low-alloy steel in a sulfurated marine atmosphere, Mater. Sci. Eng. A. 759 (2019) 124–141, doi:10.1016/j.msea.2019.05.024.

[28] T. Zhang, W. Zhao, Q. Deng, W. Jiang, Y. Wang, Y. Wang, W. Jiang, Effect of microstructure inhomogeneity on hydrogen embrittlement susceptibility of X80 welding HAZ under pressurized gaseous hydrogen, Int. J. Hydrogen Energy. 42 (2017) 25102–25113, doi:10.1016/j.ijhydene.2017.08.081.

[29] A. Zafra, J. Belzunce, C. Rodríguez, I. Fernández-Pariente, Hydrogen embrittlement of the coarse grain heat affected zone of a quenched and tempered 42CrMo4 steel, Int. J. Hydrogen Energy. 45 (2020) 16890–16908, doi:10.1016/j.ijhydene.2020.04.097.

[30] Y. Song, M. Chai, W. Wu, Y. Liu, M. Qin, G. Cheng, Experimental Investigation of the Effect of Hydrogen on Fracture Toughness of 2.25Cr-1Mo-0.25V Steel and Welds after Annealing, Materials (Basel). 11 (2018) 499. doi:10.3390/ma11040499.

[31] Y. Song, M. Chai, B. Yang, Z. Han, S. Ai, Y. Liu, G. Cheng, Y. Li, Investigation of the influence of pre-charged hydrogen on fracture toughness of as-received 2.25Cr1Mo0.25V steel and weld, Materials (Basel). 11 (2018). doi:10.3390/ma11071068.

[32] P.A.S. Pereira, C.S.G. Franco, J.L.M. Guerra Filho, D.S. Dos Santos, Hydrogen effects on the microstructure of a 2.25Cr-1Mo-0.25 v steel welded joint, in: Int. J. Hydrogen Energy, Elsevier Ltd, 2015: pp. 17136–17143. doi:10.1016/j.ijhydene.2015.07.095.

[33] V. Karthik, K. V Kasiviswanathan, K. Laha, B. Raj, Determination of gradients in mechanical properties of 2.25 Cr-1Mo weldments using shear-punch tests, Weld. JOURNAL-NEW YORK-. 81 (2002) 265-S.

[34] Y. Murakami, S. Matsuoka, Effect of hydrogen on fatigue crack growth of metals, Eng. Fract. Mech. 77 (2010) 1926–1940, doi:10.1016/j.engfracmech.2010.04.012.

[35] A. Nagao, N. Ishikawa, T. Takano, Hydrogen Compatibility and Suitability of (Ni)-Cr-Mo High-Strength Low-Alloy Seamless Line Pipe Steels for Pressure Vessels for Hydrogen Storage, in: ASME International, 2018. doi:10.1115/pvp2018-84726.

[36] J.R. Rice, A path independent integral and the approximate analysis of strain concentration by notches and cracks, J. Appl. Mech. Trans. ASME. 35 (1964) 379–388, doi:10.1115/1.3601206.

[37] I. Peñuelas, C. Betegón, C. Rodríguez, A ductile failure model applied to the determination of the fracture toughness of welded joints. Numerical simulation and experimental validation, Eng. Fract. Mech. 73 (2006) 2756–2773. doi:10.1016/j.engfracmech.2006.05.007.

[38] C. Ruggieri, R.H. Dodds, A transferability model for brittle fracture including constraint and ductile tearing effects: A probabilistic approach, Int. J. Fract. 79 (1996) 309–340, doi:10.1007/BF00018594.

[39] M.C. Burstow, I.C. Howard, R.A. Ainsworth, The influence of constraint on crack tip stress fields in strength mismatched welded joints, J. Mech. Phys. Solids. 46 (1998) 845–872, doi:10.1016/S0022-5096(97)00098-7.

[40] X. Gao, C.F. Shih, V. Tvergaard, A. Needleman, Constraint effects on the ductile-brittle transition in small scale yielding, J. Mech. Phys. Solids. 44 (1996) 1255–1271, doi:10.1016/0022-5096(96)00034-8.

[41] C. Betegón, J.W. Hancock, Two-parameter characterization of elastic-plastic crack-tip fields, J. Appl. Mech. Trans. ASME. 58 (1991) 104–110, doi:10.1115/1.2897135.

[42] C. Betegón, I. Peñuelas, A constraint based parameter for quantifying the crack tip stress fields in welded joints, Eng. Fract. Mech. 73 (2006) 1865–1877, doi:10.1016/j.engfracmech.2006.02.012.

[43] M. Dadfarnia, P. Sofronis, B.P. Somerday, I.M. Robertson, On the small scale character of the stress and hydrogen concentration fields at the tip of an axial crack in steel pipeline: Effect of hydrogen-induced softening on void growth, Int. J. Mater. Res. 99 (2008) 557–570, doi:10.3139/146.101674.

[44] P. Sofronis, R.M. McMeeking, Numerical analysis of hydrogen transport near a blunting crack tip, J. Mech. Phys. Solids. 37 (1989) 317–350, doi:10.1016/0022-5096(89)90002-1.

[45] A.H.M. Krom, R.W.J. Koers, A. Bakker, Hydrogen transport near a blunting crack tip, J. Mech. Phys. Solids. 47 (1999) 971–992.

[46] H. Kanayama, S. Ndong-Mefane, M. Ogino, R. Miresmaeili, Reconsideration of the Hydrogen Diffusion Model Using the McNabb-Foster Formulation, Mem. Fac. Eng. Kyushu Univ. 69 (2009) 149–161.

[47] C.V. Di Leo, L. Anand, Hydrogen in metals: A coupled theory for species diffusion and large elastic–plastic deformations, Int. J. Plast. 43 (2013) 42–69, doi:10.1016/j.ijplas.2012.11.005.

[48] A. Díaz, J.M. Alegre, I.I. Cuesta, Coupled hydrogen diffusion simulation using a heat transfer analogy, Int. J. Mech. Sci. 115–116 (2016), doi:10.1016/j.ijmecsci.2016.07.020.

[49] E. Martínez-Pañeda, S. del Busto, C.F. Niordson, C. Betegón, Strain gradient plasticity modeling of hydrogen diffusion to the crack tip, Int. J. Hydrogen Energy. 41 (2016) 10265–10274, doi:10.1016/J.IJHYDENE.2016.05.014.

[50] S. Kumar, I.A. Khan, V. Bhasin, R.K. Singh, Characterization of crack tip stresses in plane-strain fracture specimens having weld center crack, Int. J. Solids Struct. 51 (2014) 1464–1474, doi:10.1016/j.ijsolstr.2013.12.039.

[51] K. Poorhaydari, B.M. Patchett, D.G. Ivey, Estimation of cooling rate in the welding of plates with intermediate thickness, (n.d.).

[52] T. Moltubakk, C. Thaulow, Z.L. Zhang, Application of local approach to inhomogeneous welds. Influence of crack position and strength mismatch, Eng. Fract. Mech. 62 (1999) 445–462. doi:10.1016/s0013-7944(98)00108-8.

[53] D.M. Rodrigues, L.F. Menezes, A. Loureiro, The influence of the HAZ softening on the mechanical behaviour of welded joints containing cracks in the weld metal, Eng. Fract. Mech. 71 (2004) 2053–2064, doi:10.1016/j.engfracmech.2003.09.002.

[54] R. Singh, M.J. Alberts, S.N. Melkote, Characterization and prediction of the heat-affected zone in a laser-assisted mechanical micromachining process, Int. J. Mach. Tools Manuf. 48 (2008) 994–1004, doi:10.1016/j.ijmachtools.2008.01.004.

[55] M.L. Zhu, D.Q. Wang, F.Z. Xuan, Effect of long-term aging on microstructure and local behavior in the heat-affected zone of a Ni-Cr-Mo-V steel welded joint, Mater. Charact. 87 (2014) 45–61, doi:10.1016/j.matchar.2013.10.026.

[56] Y. Tanaka, S. Aihara, S. Konosu, K. Hayashi, M. Yuga, H. Yamamoto, N. Ohtsuka, H. Mimura, Combined effect of temper and hydrogen embrittlement on impact properties of Cr-Mo steels, in: Am. Soc. Mech. Eng. Press. Vessel. Pip. Div. PVP, American Society of Mechanical Engineers Digital Collection, 2006: pp. 555–561. doi:10.1115/PVP2006-ICPVT-11-93360.

[57] K. Prasad, D.K. Dwivedi, Microstructure and Tensile Properties of Submerged Arc Welded 1.25Cr-0.5Mo Steel Joints, Mater. Manuf. Process. 23 (2008) 463–468. doi:10.1080/10426910802103551.

[58] A. McNabb, P.K. Foster, A new analysis of the diffusion of hydrogen in iron and ferritic steels, Trans. Metall. Soc. AIME. 227 (1963) 618–627 doi:citeulike-article-id:4956272.

[59] J. Toribio, V. Kharin, A generalised model of hydrogen diffusion in metals with multiple trap types, Philos. Mag. (2015) 1–23. doi:10.1080/14786435.2015.1079660.

[60] A. Díaz, I.I. Cuesta, E. Martinez-Pañeda, J.M. Alegre, Analysis of hydrogen permeation tests considering two different modelling approaches for grain boundary trapping in iron, Int. J. Fract. (2019), doi:10.1007/s10704-019-00411-8.

[61] L. Vecchi, H. Simillion, R. Montoya, D. Van Laethem, E. Van den Eeckhout, K. Verbeken, H. Terryn, J. Deconinck, Y. Van Ingelgem, Modelling of hydrogen permeation experiments in iron alloys: Characterization of the accessible parameters – Part I - The entry side, Electrochim. Acta. 262 (2018) 57–65, doi:10.1016/J.ELECTACTA.2017.12.172.

[62] Q. Liu, A.D. Atrens, Z. Shi, K. Verbeken, A. Atrens, Determination of the hydrogen fugacity during electrolytic charging of steel, Corros. Sci. 87 (2014) 239–258, doi:10.1016/J.CORSCI.2014.06.033.

[63] R.O. J.C.M. Li L.S. Darken, The thermodynamics of stressed solids, Z. Phys. Chem., 49 (1966), Pp. 271–29. (1966).

[64] A. Díaz, J.M. Alegre, I.I. Cuesta, A review on diffusion modelling in hydrogen related failures of metals, Eng. Fail. Anal. 66 (2016), doi:10.1016/j.engfailanal.2016.05.019.

[65] R.A. Oriani, The diffusion and trapping of hydrogen in steel, Acta Metall. 18 (1970) 147–157, doi:10.1016/0001-6160(70)90078-7.

[66] M. Dadfarnia, P. Sofronis, T. Neeraj, Hydrogen interaction with multiple traps: Can it be used to mitigate embrittlement?, Int. J. Hydrogen Energy. 36 (2011) 10141–10148, doi:10.1016/j.ijhydene.2011.05.027.

[67] M. Dadfarnia, M.L. Martin, A. Nagao, P. Sofronis, I.M. Robertson, Modeling hydrogen transport by dislocations, J. Mech. Phys. Solids. 78 (2014) 511–525, doi:10.1016/j.jmps.2015.03.002.
[68] A.M. Krom, A. Bakker, Hydrogen trapping models in steel, Metall. Mater. Trans. B. 31 (2000) 1475–1482, doi:10.1007/s11663-000-0032-0.
[69] A. Taha, P. Sofronis, A micromechanics approach to the study of hydrogen transport and embrittlement, Eng. Fract. Mech. 68 (2001) 803–837, doi:10.1016/S0013-7944(00)00126-0.
[70] T. Hajilou, Y. Deng, B.R. Rogne, N. Kheradmand, A. Barnoush, In situ electrochemical microcantilever bending test: A new insight into hydrogen enhanced cracking, Scr. Mater. 132 (2017) 17–21, doi:10.1016/j.scriptamat.2017.01.019.
[71] C. San Marchi, T. Michler, K.A. Nibur, B.P. Somerday, On the physical differences between tensile testing of type 304 and 316 austenitic stainless steels with internal hydrogen and in external hydrogen, Int. J. Hydrogen Energy. 35 (2010) 9736–9745. doi:10.1016/j.ijhydene.2010.06.018.
[72] A. Turnbull, Perspectives on hydrogen uptake, diffusion and trapping, Int. J. Hydrogen Energy. (2015), doi:10.1016/j.ijhydene.2015.06.147.
[73] E. Martínez-Pañeda, A. Díaz, L. Wright, A. Turnbull, Generalised boundary conditions for hydrogen transport at crack tips, Corros. Sci. 173 (2020) 108698, doi:10.1016/j.corsci.2020.108698.
[74] C.-S. Oh, Y.-J. Kim, Coupled analysis of hydrogen transport within abaqus, Trans. Korean Soc. Mech. Eng. A. 33 (2009) 600–606.
[75] A. Raina, V.S. Deshpande, N.A. Fleck, Analysis of electro-permeation of hydrogen in metallic alloys, Philos. Trans. A. Math. Phys. Eng. Sci. 375 (2017) 20160409, doi:10.1098/rsta.2016.0409.
[76] A.J. Kumnick, H.H. Johnson, Deep trapping states for hydrogen in deformed iron, Acta Metall. 28 (1980) 33–39, doi:10.1016/0001-6160(80)90038-3.
[77] L.B. Peral, A. Zafra, I. Fernández-Pariente, C. Rodríguez, J. Belzunce, Effect of internal hydrogen on the tensile properties of different CrMo(V) steel grades: Influence of vanadium addition on hydrogen trapping and diffusion, Int. J. Hydrogen Energy. 45 (2020) 22054–22079, doi:10.1016/j.ijhydene.2020.05.228.
[78] E. Martínez-Pañeda, C.F. Niordson, R.P. Gangloff, Strain gradient plasticity-based modeling of hydrogen environment assisted cracking, Acta Mater. 117 (2016) 321–332, doi:10.1016/J.ACTAMAT.2016.07.022.